Large-Scale Response of the Tropical Atmosphere to Transient Convection

PEDRO L. SILVA DIAS[1]

National Center for Atmospheric Research,[2] Boulder, CO 80307

WAYNE H. SCHUBERT AND MARK DEMARIA

Department of Atmospheric Science, Colorado State University, Fort Collins, CO 80523

(Manuscript received 7 February 1983, in final form 15 July 1983)

ABSTRACT

We consider the problem of the linear response of a stratified, equatorial, β-plane model atmosphere to specified transient sources of heat and momentum. The method of solution involves transforms in all three spatial coordinates. A finite Stürm-Liouville transform is used in z, a Fourier transform in x, and a generalized Hermite transform in y. The resulting spectral equations can then be solved analytically for a specified forcing. Of particular interest is the case of a Gaussian-shaped heat source centered at latitude y_o and with e-folding radius a. The heat source is transient and has time scale $1/\alpha$. Using the Parceval relation we compute how the forced energy is partitioned between Kelvin, mixed Rossby–gravity, Rossby and gravity modes as a function of a, y_o, α. Model results using a heat source centered at 11°S with an e-folding radius of 750 km and a time scale of about a day indicate that many aspects of the summertime upper tropospheric circulation over South America can be explained by the dispersive properties of Rossby and mixed Rossby–gravity waves. These results also show that the transient heat source excites Kelvin waves which propagate rapidly eastward as a nondispersive wave group. The existence of the Kelvin waves has implications for the initialization of tropical forecast models. By applying a nonlinear normal mode initialization procedure in the middle of a model simulation we investigate how the initialization distorts the subsequent evolution. Much of the distortion is associated with the Kelvin wave response.

1. Introduction

Although the zonally symmetric Hadley cell provides a first approximation to the tropical circulation, there also exist large east–west asymmetric circulations associated with the equatorial continental areas of Africa, South America and the region near Indonesia and New Guinea. Over these regions, both the convective activity and the tropospheric circulation fluctuate diurnally and also on time scales of days or longer.

An example of an east–west asymmetry in the tropical circulation can be seen in Fig. 1 (adapted from Kreuels *et al.*, 1975), which shows the average 200 and 700 mb flow over South America for four winters (June–August) and four summers (December–February) between 1966 and 1970. Also shown are the long-term rainfall patterns for winter and summer. The most striking feature of Fig. 1 is the difference between the nearly zonal upper tropospheric flow over Brazil in winter and the strong anticyclone in summer. According to Kreuels *et al.* (1975) the summertime anticyclone (the Bolivian high) appears as a closed feature above 300 mb and is coupled to the trough toward the east. Because summertime precipitation over the Amazon basin is much larger than wintertime precipitation, one obvious possibility is that the upper tropospheric anticyclone is maintained by the release of latent heat.

The circulation pattern over South America also varies on time scales shorter than the seasonal variation shown in Fig. 1. For example, a study by Virgi (1981) of the tropospheric circulation over South America using satellite derived cloud winds shows that the maximum wind, vorticity and divergence can attain values much above the average and that the position of the Bolivian high can vary significantly. Kousky (1979) has shown that some of the variability of cloudiness and convective activity can be explained by the influence of midlatitude systems that penetrate to low latitudes over Brazil. In a recent study of the transient aspects of the upper tropospheric circulation, Kousky and Gan (1981) found that upper cold lows often form in summer around 35°W, drift westward and play a significant role in the precipitation pattern over Brazil. We can summarize by saying that the convective activity and circulation over the Amazon region varies on time scales ranging from the annual movement of

[1] On leave from Instituto Astronomico e Geofisico Universidade de Sao Paulo, Brazil.

[2] The National Center for Atmospheric Research is sponsored by the National Science Foundation.

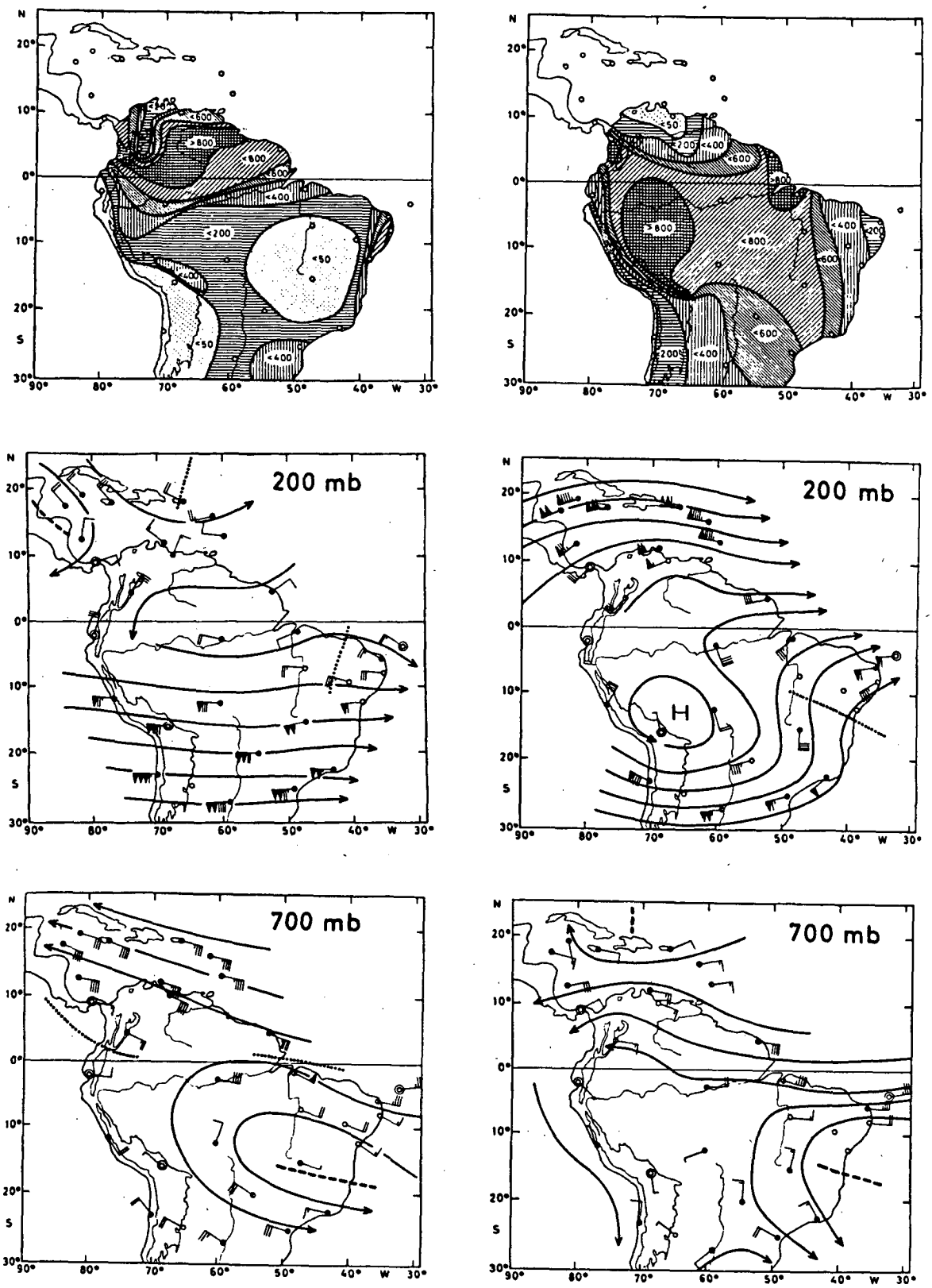

FIG. 1. Streamline patterns at 700 and 200 mb and rainfall in millimeters. The left column is for winter (June–August) and the right column for summer (December–February). Note the striking difference in Amazon basin rainfall and upper tropospheric circulation between summer and winter. This figure has been adapted from the work of Kreuels *et al.* (1975).

the ITCZ through the synoptic to the diurnal (see Kousky, 1980).

Although certain aspects of low-latitude atmospheric response to transient forcing can be studied using an f-plane model such as the one developed by Paegle (1978), the problem at hand would appear to require an equatorial model. The simplest such model is the equatorial β-plane model described by Matsuno (1966) and Lindzen (1967). The use of equatorial β-plane models has a brief but rich history in both meteorology and oceanography. For example, steady-state and long-term atmospheric response to convective forcing has been studied by Webster (1972, 1973a,b, 1981), Gill (1980) and Geisler and Stevens (1982), while the transient response to midlatitude cold surges toward the South China Sea has been studied by Lim and Chang (1981) and Lau and Lim (1982). For an extensive review of the use of equatorial β-plane models in geophysical fluid dynamics the reader is referred to Chapter 11 of Gill (1982).

In the present paper, the atmospheric response to localized transient heat sources which simulate convective bursts in the tropical region is studied. The model development begins with the linearized equations for a stratified fluid on the equatorial β-plane. In Section 2, a finite Stürm-Liouville transform is applied in the vertical, which reduces the governing equations to a series of shallow water equations which determine the horizontal structure of each vertical mode. From this point on, the emphasis is placed on the horizontal structure of the solution for a single vertical mode (the mode which is most excited by the heating). The horizontal structure equations with transient forcing are then solved in a fashion similar to that described by Cane and Sarachik (1976) for an oceanographic problem. The energy partition between rotational and gravitational modes as a function of the latitude, horizontal scale and time scale of the heat source is considered in Section 3. In Section 4, results of a model simulation using a heat source centered at 11°S with an e-folding radius of 750 km and a time scale of about a day are presented. These results are used to explain some observed features of the Bolivian high revealed in 200 mb FGGE maps from February 1979. The "fast mode" response in these simulations raises questions about subsequent distortion which would result from the use of a nonlinear normal mode initialization during the period of forcing. This is discussed in Section 5.

2. Governing equations

Consider a compressible hydrostatic fluid which lies above an equatorial β-plane and which is forced by known sources and sinks of momentum and heat. Using $z = \ln(p_o/p)$, where p_o is a constant "surface" pressure, as the vertical coordinate, we can write the governing equations as

$$\frac{\partial u}{\partial t} + u\frac{\partial u}{\partial x} + v\frac{\partial u}{\partial y} + w\frac{\partial u}{\partial z} - \beta y v + \frac{\partial \phi}{\partial x} = F, \quad (2.1)$$

$$\frac{\partial v}{\partial t} + u\frac{\partial v}{\partial x} + v\frac{\partial v}{\partial y} + w\frac{\partial v}{\partial z} + \beta y u + \frac{\partial \phi}{\partial y} = G, \quad (2.2)$$

$$\frac{\partial \phi}{\partial z} - RT = 0, \quad (2.3)$$

$$\frac{\partial u}{\partial x} + \frac{\partial v}{\partial y} + \frac{\partial w}{\partial z} - w = 0, \quad (2.4)$$

$$\frac{\partial T}{\partial t} + u\frac{\partial T}{\partial x} + v\frac{\partial T}{\partial y} + \left(\frac{\partial T}{\partial z} + \kappa T\right)w = \frac{Q}{c_p}, \quad (2.5)$$

where u is the eastward component of velocity, v the northward component, w the vertical log pressure velocity, ϕ the geopotential, T the temperature, β the equatorial value of the northward gradient of the Coriolis parameter, and F, G and Q the known momentum and heat source/sink terms.

Linearizing about a basic state of rest and combining (2.3)–(2.5) yields

$$\frac{\partial u}{\partial t} - \beta y v + \frac{\partial \phi}{\partial x} = \frac{\partial \tilde{u}}{\partial t}, \quad (2.6)$$

$$\frac{\partial v}{\partial t} + \beta y u + \frac{\partial \phi}{\partial y} = \frac{\partial \tilde{v}}{\partial t}, \quad (2.7)$$

$$\frac{\partial}{\partial t}\left[e^z \frac{\partial}{\partial z}\left(\frac{e^{-z}}{R\Gamma}\frac{\partial \phi}{\partial z}\right)\right] - \left(\frac{\partial u}{\partial x} + \frac{\partial v}{\partial y}\right) = \frac{\partial}{\partial t}\left[e^z \frac{\partial}{\partial z}\left(\frac{e^{-z}}{R\Gamma}\frac{\partial \tilde{\phi}}{\partial z}\right)\right], \quad (2.8)$$

where $\Gamma(z) = d\bar{T}/dz + \kappa\bar{T}$ is the basic state static stability and $\partial\tilde{u}/\partial t = F$, $\partial\tilde{v}/\partial t = G$, $\partial(\partial\tilde{\phi}/\partial z)/\partial t = RQ/c_p$ are the momentum and heat source/sink terms ($\tilde{\phi} = 0$ at $z = 0$). At the upper boundary we require that the vertical log pressure velocity vanish, while at the lower boundary (approximated by the $z = 0$ surface) we require that the actual vertical velocity vanish. Expressing these boundary conditions in terms of ϕ, we obtain

$$\frac{\partial}{\partial t}\left[\frac{\partial}{\partial z}(\phi - \tilde{\phi})\right] = 0, \quad z = z_T, \quad (2.9a)$$

$$\frac{\partial}{\partial t}\left[\frac{\partial}{\partial z}(\phi - \tilde{\phi}) - \frac{\Gamma}{\bar{T}}(\phi - \tilde{\phi})\right] = 0, \quad z = 0. \quad (2.9b)$$

Our system of equations is now (2.6)–(2.8) subject to boundary conditions (2.9). We shall solve this problem using transform techniques. A finite Stürm-Liouville transform with kernel $\Psi_n(z)$ and weight $e^{-z/2}$ will be used in the vertical. This transform and its inverse can be written as

$$f_n(x, y, t) = \int_0^{z_T} f(x, y, z, t)\Psi_n(z)e^{-z/2}dz, \quad (2.10)$$

$$f(x, y, z, t) = \sum_{n=0}^{\infty} f_n(x, y, t)\Psi_n(z)e^{z/2}, \quad (2.11)$$

where $f(x, y, z, t)$ can represent u, v, ϕ, $\tilde{u}$, $\tilde{v}$ or $\tilde{\phi}$. The kernel Ψ_n of this transform, which is derived in Appendix A, has been designed to conveniently transform the first and last terms in (2.8), subject to boundary conditions (2.9).

Taking the vertical transform of (2.6)–(2.8) and using the operational relation (A5) we obtain

$$\frac{\partial u_n}{\partial t} - \beta y v_n + \frac{\partial \phi_n}{\partial x} = \frac{\partial \tilde{u}_n}{\partial t}, \quad (2.12)$$

$$\frac{\partial v_n}{\partial t} + \beta y u_n + \frac{\partial \phi_n}{\partial y} = \frac{\partial \tilde{v}_n}{\partial t}, \quad (2.13)$$

$$\frac{\partial \phi_n}{\partial t} + c_n^2\left(\frac{\partial u_n}{\partial x} + \frac{\partial v_n}{\partial y}\right) = \frac{\partial \tilde{\phi}_n}{\partial t}, \quad (2.14)$$

which are identical to the governing equations for the divergent barotropic model (i.e., the shallow water equations) with pure gravity wave speed $c_n = (gh_n)^{1/2}$. Since the equivalent depths h_n are determined from the eigenvalues of (A4), they depend on the static stability $\Gamma(z)$, the height of the upper boundary z_T and, to a lesser extent, on the reference temperature $\bar{T}$ at $z = 0$.

Perhaps the least controversial way to proceed would be to set z_T to a value which corresponds to a pressure of a few millibars, solve (A4) using a standard atmosphere $\bar{T}$ and $\Gamma(z)$, project observed (i.e. diagnostically determined) tropical (e.g., Amazon Basin) profiles of $\tilde{u}$, $\tilde{v}$, $\tilde{\phi}$ onto the vertical modes using (2.10), solve the horizontal structure equation sets (2.12)–(2.14) using $\{\tilde{u}_n, \tilde{v}_n, \tilde{\phi}_n, n = 0, 1, \ldots, N\}$ as forcing, and finally, reconstruct the physical space field u, v, ϕ from (2.11). If the momentum and heat sources were confined below the tropopause, simulations out to many days would be possible before false reflections from the distant upper lid had any effect on the tropospheric part of the solution. In the present calculations we have opted for the simpler alternative of including only one term in the summation (2.11). This approach is in the spirit of Gill (1980), who has argued that important contributions to the total solution in physical space will be from vertical modes whose vertical scale is the same order as the vertical scale of the forcing. According to Gill, the important contributions from convective heating should be centered around $c_n \approx 60$ m s^{-1}. For an idealized heating profile, a constant static stability and a rigid lid at $\sim$3 mb, Geisler and Stevens (1982, Fig. 2) have computed a vertical mode projection which centers around $c_n \approx 40$ m s^{-1}. They have also pointed out that for complete quantitative discussions, a summation over vertical modes is required. Here we shall not undertake such a complete quantitative analysis, but will discuss only certain qualitative aspects of the problem. This concentration on only one vertical mode allows us to nondimensionalize the single horizontal structure set and thus simplify the following mathematical development.

Two other possible interpretations of the above single vertical mode procedure are that we are dealing with the response of a standard two-level model with no external mode or that we are dealing with the first internal mode of a multi-level model with a lid at 100 mb. For such a multi-level model, S. Fulton (personal communication, 1982) has solved the Stürm-Liouville problem [Eq. (A4)] using the mean Marshall Islands sounding of Yanai *et al.* (1973) and with the upper boundary condition (A4c) applied at 100 mb. The resulting values of c_n for the external and first two in-

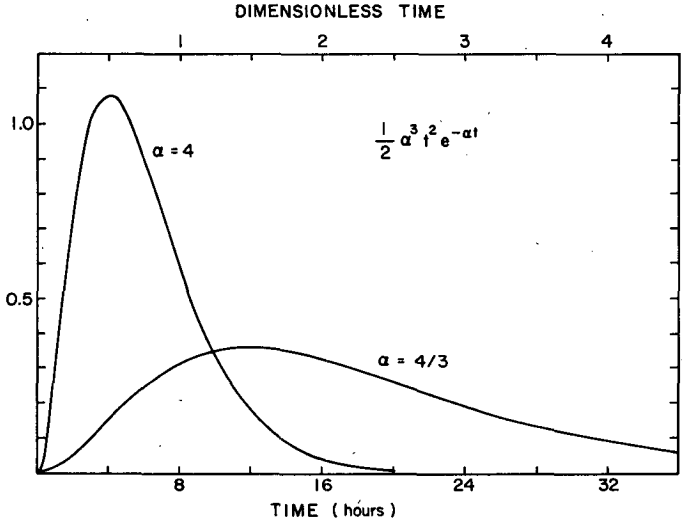

FIG. 2. Time dependence of the momentum and heat source/sink terms for two values of the parameter α.

ternal modes are, respectively, 287.3, 51.2 and 29.4 m s^{-1}. Fulton has also computed how the $\tilde{\phi}$ which results from Yanai's apparent heat source profile projects onto the various vertical modes. In terms of the total available potential energy generated by the apparent heat source, over 90% ends up in the first internal mode. Based on this result we shall use 51 m s^{-1} as our single value of c_n. Thus, the results shown in later sections on thermally forced motions are essentially the small-amplitude response that would be calculated with a GCM having a lid at 100 mb and with a specified heat source profile in agreement with Yanai's Marshall Islands data[3].

It is now convenient to convert (2.12)–(2.14) into nondimensional form by choosing as the unit of time $[T] = (1/c_n\beta)^{1/2}$, the unit of horizontal distance $[L] = (c_n/\beta)^{1/2}$ and the unit of vertical distance h_n. The horizontal length scale $[L]$ can be interpreted as the usual Rossby radius of deformation $\lambda = c_n/f$ evaluated at $y = [L]$, i.e. $[L] = \lambda([L]) = c_n/\beta[L]$. Similarly, $[T]$ is the inverse of the Coriolis parameter at $y = [L]$ (Cane and Sarachik, 1976). Using the same symbols x, y, t for the new dimensionless independent variables, u, v, ϕ for the new dimensionless dependent variables, and $\tilde{u}, \tilde{v}, \tilde{\phi}$ for the space-dependent part of the source/sink terms, Eqs. (2.12)–(2.14) become

$$\frac{\partial \mathbf{W}}{\partial t} + \mathbf{L}\mathbf{W} = \tilde{\mathbf{W}}\tfrac{1}{2}\alpha^3 t^2 e^{-\alpha t}, \tag{2.15}$$

where

$$\mathbf{W} = \begin{pmatrix} u \\ v \\ \phi \end{pmatrix}, \quad \tilde{\mathbf{W}} = \begin{pmatrix} \tilde{u} \\ \tilde{v} \\ \tilde{\phi} \end{pmatrix}, \quad \mathbf{L} = \begin{pmatrix} 0 & -y & \dfrac{\partial}{\partial x} \\ y & 0 & \dfrac{\partial}{\partial y} \\ \dfrac{\partial}{\partial x} & \dfrac{\partial}{\partial y} & 0 \end{pmatrix}. \tag{2.16}$$

Here we have assumed that the time-dependent part of the source/sink terms is given by $\frac{1}{2}\alpha^3 t^2 e^{-\alpha t}$. Small values of the dimensionless parameter α correspond to slow forcing and large values to rapid forcing (see Fig. 2), but the total forcing is independent of α since

$$\int_0^\infty \frac{1}{2}\alpha^3 t^2 e^{-\alpha t} dt = 1.$$

Defining $\hat{\mathbf{W}}(k, y, t)$ as the Fourier transform of $\mathbf{W}(x, y, t)$ we can write the Fourier transform pair as

$$\hat{\mathbf{W}}(k, y, t) = \frac{1}{(2\pi)^{1/2}} \int_{-\infty}^{\infty} \mathbf{W}(x, y, t) e^{-ikx} dx, \tag{2.17}$$

$$\mathbf{W}(x, y, t) = \frac{1}{(2\pi)^{1/2}} \int_{-\infty}^{\infty} \hat{\mathbf{W}}(k, y, t) e^{ikx} dk, \tag{2.18}$$

with similar expressions for $\hat{\tilde{\mathbf{W}}}(k, y)$ and $\tilde{\mathbf{W}}(x, y)$. Fourier transforming (2.15) we obtain

$$\frac{\partial \hat{\mathbf{W}}}{\partial t} + \hat{\mathbf{L}}\hat{\mathbf{W}} = \hat{\tilde{\mathbf{W}}}\tfrac{1}{2}\alpha^3 t^2 e^{-\alpha t}, \tag{2.19}$$

where $\hat{\mathbf{L}}$ is identical to $\mathbf{L}$ but with $\partial/\partial x$ replaced by ik.

Our next task is to transform (2.19) in y. We consider the complex three-component vectors $\mathbf{f}$ and $\mathbf{g}$, all the components of which go to zero as $y \to \pm\infty$. The inner product of $\mathbf{f}$ and $\mathbf{g}$ is defined as

$$(\mathbf{f}, \mathbf{g}) = \int_{-\infty}^{\infty} (f_1 g_1^* + f_2 g_2^* + f_3 g_3^*) dy, \tag{2.20}$$

where $(\ )^*$ denotes the complex conjugate. We now introduce the meridional transform pair

$$W_{m,r}(k, t) = (\hat{\mathbf{W}}(k, y, t), \mathbf{K}_{m,r}(k, y)), \tag{2.21}$$

$$\hat{\mathbf{W}}(k, y, t) = \sum_{m,r} W_{m,r}(k, t)\mathbf{K}_{m,r}(k, y), \tag{2.22}$$

where $\mathbf{K}_{m,r}(k, y)$ is a complex, three-component, time-independent vector kernel which satisfies

$$\hat{\mathbf{L}}\mathbf{K}_{m,r} + i\nu_{m,r}\mathbf{K}_{m,r} = 0. \tag{2.23}$$

The adjoint of $\hat{\mathbf{L}}$ with respect to the inner product (2.20) is an operator $\hat{\mathbf{L}}^\dagger$ which satisfies

$$(\hat{\mathbf{L}}\mathbf{f}, \mathbf{g}) = (\mathbf{f}, \hat{\mathbf{L}}^\dagger \mathbf{g}) \tag{2.24}$$

for all $\mathbf{f}$ and $\mathbf{g}$ satisfying the boundary conditions. We can show (see Appendix B) that the operator $\hat{\mathbf{L}}$ is skew-Hermitian (i.e., $\hat{\mathbf{L}}^\dagger = -\hat{\mathbf{L}}$) so that (2.24) becomes

$$(\hat{\mathbf{L}}\mathbf{f}, \mathbf{g}) = -(\mathbf{f}, \hat{\mathbf{L}}\mathbf{g}). \tag{2.25}$$

As shown by Kasahara (1977), an analogous relation holds in the spherical case. Since $\hat{\mathbf{L}}$ is skew-Hermitian, the eigenvalues $\nu_{m,r}$ of (2.23) are real and the eigenfunctions $\mathbf{K}_{m,r}$ are orthogonal as long as degeneracy does not occur. The eigenvalues and eigenfunctions of (2.23) have been thoroughly discussed by Matsuno (1966) and Cane and Sarachik (1976). For a summary of the results relevant here, see Appendix B. Taking the inner product of (2.19) with $\mathbf{K}_{m,r}$ we obtain

$$\left(\frac{\partial \hat{\mathbf{W}}}{\partial t}, \mathbf{K}_{m,r}\right) + (\hat{\mathbf{L}}\hat{\mathbf{W}}, \mathbf{K}_{m,r}) = (\hat{\tilde{\mathbf{W}}}, \mathbf{K}_{m,r})\tfrac{1}{2}\alpha^3 t^2 e^{-\alpha t}. \tag{2.26}$$

Using (2.21), (2.23) and (2.25) we can rewrite (2.26) as

$$\frac{dW_{m,r}}{dt} - i\nu_{m,r}W_{m,r} = \tilde{W}_{m,r}\tfrac{1}{2}\alpha^3 t^2 e^{-\alpha t}. \tag{2.27}$$

[3] It should be noted that apparent heat source profiles for different geographical regions can show considerable differences, as evidenced by comparing average Marshall Islands and GATE profiles. To our knowledge, the vertical structure of the apparent heat source over the Amazon Basin has yet to be determined.

The solution of (2.27) is

$$W_{m,r}(k, t) = \frac{\alpha^3}{(\alpha + i\nu_{m,r})^3} \tilde{W}_{m,r}(k)e^{i\nu_{m,r}t} \times \{1 - [1 + (\alpha + i\nu_{m,r})t + \tfrac{1}{2}(\alpha + i\nu_{m,r})^2t^2] \times e^{-(\alpha+i\nu_{m,r})t}\}. \quad (2.28)$$

We can now summarize the procedure for obtaining the solution $\mathbf{W}(x, y, t)$. First, the specified forcing $\tilde{\mathbf{W}}(x, y)$ is transformed to spectral space using (2.17) and (2.21). The right-hand side of (2.28) is then computed to obtain $W_{m,r}(k, t)$, the solution in spectral space. Finally, we use (2.22) and (2.18) to transform back to physical space.

3. Energy partition

The vertically transformed equations (2.15) have the energy equation

$$\frac{\partial}{\partial t}\int_{-\infty}^{\infty}\int_{-\infty}^{\infty}(u^2 + v^2 + \phi^2)dxdy = \alpha^3t^2e^{-\alpha t}\int_{-\infty}^{\infty}\int_{-\infty}^{\infty}(u\tilde{u} + v\tilde{v} + \phi\tilde{\phi})dxdy, \quad (3.1)$$

which relates the time change of total energy to the generation by the specified momentum and thermal forcing. The total energy can be computed from the solution in physical space or from the solution in spectral space using the Parseval relation

$$\int_{-\infty}^{\infty}\int_{-\infty}^{\infty}(u^2 + v^2 + \phi^2)dxdy = \int_{-\infty}^{\infty}\sum_{m=-1}^{\infty}\sum_{r=0}^{2}|W_{m,r}(k, t)|^2dk, \quad (3.2)$$

where $W_{m,r}(k, t)$ is given by (2.28). From (2.28) we note that the amplitude of $W_{m,r}$ changes with time. For large t the factor $e^{-\alpha t}$ becomes small compared to unity, and in the limit $t \to \infty$ we obtain

$$|W_{m,r}(k, \infty)|^2 = \left(\frac{\alpha^2}{\alpha^2 + \nu_{m,r}^2}\right)^3|\tilde{W}_{m,r}(k)|^2. \quad (3.3)$$

The above equation is valid after the forcing becomes negligible and the amplitude of $W_{m,r}$ becomes constant with time. The final amplitude of $W_{m,r}$ depends on the time scale of the forcing compared to the frequency of a given mode. For very rapid forcing, the term involving α becomes close to unity, and in the limit as $\alpha \to \infty$, $|W_{m,r}(k, \infty)|^2$ becomes $|\tilde{W}_{m,r}(k)|^2$. The limiting case $\alpha \to \infty$ is equivalent to impulsive forcing where all the momentum and/or heat is added instantaneously. The total energy generated in this case is given by

$$T_I = \int_{-\infty}^{\infty}\sum_{m=-1}^{\infty}\sum_{r=0}^{2}|\tilde{W}_{m,r}(k)|^2dk. \quad (3.4)$$

The term involving α in (3.3) increases as α increases, so the total energy generated is a maximum for the case of impulsive forcing. Since the solution technique we have used is equivalent to a normal mode expansion, many characteristics of the solution can be inferred from the partition of energy between the different modes. In order to measure the partition of energy at a particular time, the following definitions are made:

$$T = \frac{1}{T_I}\int_{-\infty}^{\infty}\sum_{m=-1}^{\infty}\sum_{r=0}^{2}|W_{m,r}(k, t)|^2dk, \quad (3.5)$$

$$K = \frac{1}{T_I}\int_{-\infty}^{\infty}|W_{-1,2}(k, t)|^2dk, \quad (3.6)$$

$$\text{MRG} = \frac{1}{T_I}\int_{-\infty}^{\infty}\sum_{r=0}^{1}|W_{0,r}(k, t)|^2dk, \quad (3.7)$$

$$R = \frac{1}{T_I}\int_{-\infty}^{\infty}\sum_{m=1}^{\infty}|W_{m,0}(k, t)|^2dk, \quad (3.8)$$

$$G = \frac{1}{T_I}\int_{-\infty}^{\infty}\sum_{\substack{m=0\\ r=1,m>0}}^{\infty}\sum_{r=2,m=0}^{2}|W_{m,r}(k, t)|^2dk. \quad (3.9)$$

The above parameters are measures of the total energy, the energy associated with the Kelvin modes, mixed Rossby–gravity modes, Rossby modes and gravity modes respectively. Each parameter is normalized by the total energy for the case of impulsive forcing.

Eq. (2.28) gives the solution of the transformed governing equations for arbitrary spatial dependence of the forcing terms. We now consider the case where the nondimensional, vertically projected forcing terms in (2.15) are given by $\tilde{u}(x, y) = \tilde{v}(x, y) = 0$ and

$$\tilde{\phi}(x, y) = \frac{1}{\pi a^2}\exp\left[-\left(\frac{x}{a}\right)^2 - \left(\frac{y - y_0}{a}\right)^2\right]. \quad (3.10)$$

Thus, we have a heat source centered at a distance y_0 from the equator, with an e-folding radius a. The "total heating" is independent of y_0 and a since (3.10) implies $\int_{-\infty}^{\infty}\int_{-\infty}^{\infty}\tilde{\phi}(x, y)dxdy = 1$. Using (3.10), (2.17), (2.20), (2.21) and (B.4) we find that the transformed forcing is given by[4]

[4] The Hermite transforms required here can be found in Erdelyi *et al.* (1954), Vol. 2, pp. 288 and 290.

$$\tilde{W}_{m,r}(k) = \frac{\exp\left(-\frac{y_0^2}{2+a^2}\right)}{\pi(4+2a^2)^{1/2}} \left\{ \begin{array}{ll} \frac{1}{\sqrt{E_{m,r}(k)}} \exp\left(-\frac{k^2a^2}{4}\right)[\tfrac{1}{2}(\nu_{m,r}-k)B_{m+1} - m(\nu_{m+1}+k)B_{m-1}], & m \geq 0, \\ & k \neq 0 \quad \text{when} \quad r = 0 \\ \frac{1}{\sqrt{E_{m,0}(k)}}[-\tfrac{1}{2}B_{m+1} - (m+1)B_{m-1}], & m \geq 0, \\ & k = r = 0 \\ \frac{1}{\sqrt{2\pi^{1/2}}} \exp\left(-\frac{k^2a^2}{4}\right)B_0, & m = -1, \\ & r = 2 \end{array} \right\}, \quad (3.11)$$

where

$$B_m = \left\{ \begin{array}{ll} \left(\frac{2-a^2}{2+a^2}\right)^{m/2} H_m\left(\frac{2y_0}{\sqrt{4-a^4}}\right), & a \neq \sqrt{2} \\ y_0{}^m, & a = \sqrt{2} \end{array} \right\}. \quad (3.12)$$

As can be seen from (3.11) the transform of the forcing contains a factor $\exp(-k^2a^2/4)$. The e-folding half width of the Fourier spectrum is then $k = 2/a$ so that a narrow initial condition (small a) projects onto a broad band of zonal waves while a wide initial condition (large a) projects onto a narrow band of zonal waves. The factor B_m which arises from the transform in y indicates that $\tilde{W}_{m,k}(k)$ will have an oscillatory behavior as m increases.

If we now substitute (3.11) into (2.28) and the result into (3.5)–(3.9) we can compute the modal energy partition for any a, y_0, α at any time t. Fig. 3 shows the modal energy partition for $t \to \infty$ as a function of the spatial scale of the forcing (a) for two different values of y_0 and α. In Fig. 3 the Rossby wave energy increases as the spatial scale of the forcing increases. For increasing a, the disturbance which results from the forcing should then have a larger amplitude in the local region near the forcing, since the Rossby modes have low frequencies and are slowly dispersive. Comparing Fig. 3a with 3c and Fig. 3b with 3d, the Rossby wave energy also increases as the latitude of the forcing increases.

Comparison of Fig. 3a with 3b, and Fig. 3c with 3d shows the effect of the time scale on the forcing. The forcing is a maximum when $t = 2/\alpha$, which corresponds to ~4 h for $\alpha = 4$ and ~12 h for $\alpha = \frac{4}{3}$, using the time scale for the first internal mode. As can be seen from (3.3), the amplitude of a given mode is reduced when the frequency is close to α. As α decreases, the forcing excites less energy in the high-frequency modes. In Fig. 3, as α decreases, there is much less energy in the Kelvin modes, the mixed Rossby–gravity modes, and the gravity modes. For the time scale of the forcing considered here, the frequencies of the Rossby modes are much less than α, so the Rossby mode energy remains approximately constant. These results show that as the forcing becomes more rapid, the amount of gravity wave energy generated increases while the amount of Rossby wave energy generated remains approximately constant.

The amount of energy in the higher frequency modes is also dependent on the spatial scale of the forcing. For a fixed α, the energy in the high-frequency modes increases with a, reaches a maximum and decreases again. For large a, the decrease in gravity wave energy is related to the classical result from geostrophic adjustment which indicates that a disturbance in the mass field will excite less gravity wave energy and more energy in the geostrophically balanced flow as the scale of the disturbance increases. The decrease in gravity wave energy for small a is related to the time scale of the forcing. As discussed previously, when a is small, the forcing will be projected onto a wide range of zonal waves. The forcing is then projected onto higher and higher frequency gravity and Kelvin modes. From (3.3), for a given α, the amplitudes of high-frequency modes are greatly reduced. This accounts for the peaks in Fig. 3 for the Kelvin and gravity modes.

Comparing Fig. 3a with 3c and Fig. 3b with 3d, it can be seen that the amount of gravity wave energy excited does not vary strongly as a function of latitude, but the Kelvin wave energy increases with decreasing latitude while the mixed Rossby–gravity wave energy decreases with decreasing latitude. These are expected results since the gravity waves are not strongly affected by the earth's rotation, while the Kelvin wave is trapped near the equator. The mixed Rossby–gravity wave energy is exactly zero when $y_0 = 0$ since the forcing is in the mass field and is symmetric about the equator, but the mass field of the mixed Rossby–gravity wave is antisymmetric about the equator. In Fig. 3, the amount of energy in the Kelvin modes is quite striking. In many cases, the Kelvin wave energy exceeds the Rossby wave energy. Since Kelvin waves propagate toward the east and are nondispersive, a large response to the east side of the forcing should appear.

4. Simulation of upper tropospheric circulations

In the previous section we have considered the energy partition associated with transient thermal forcing

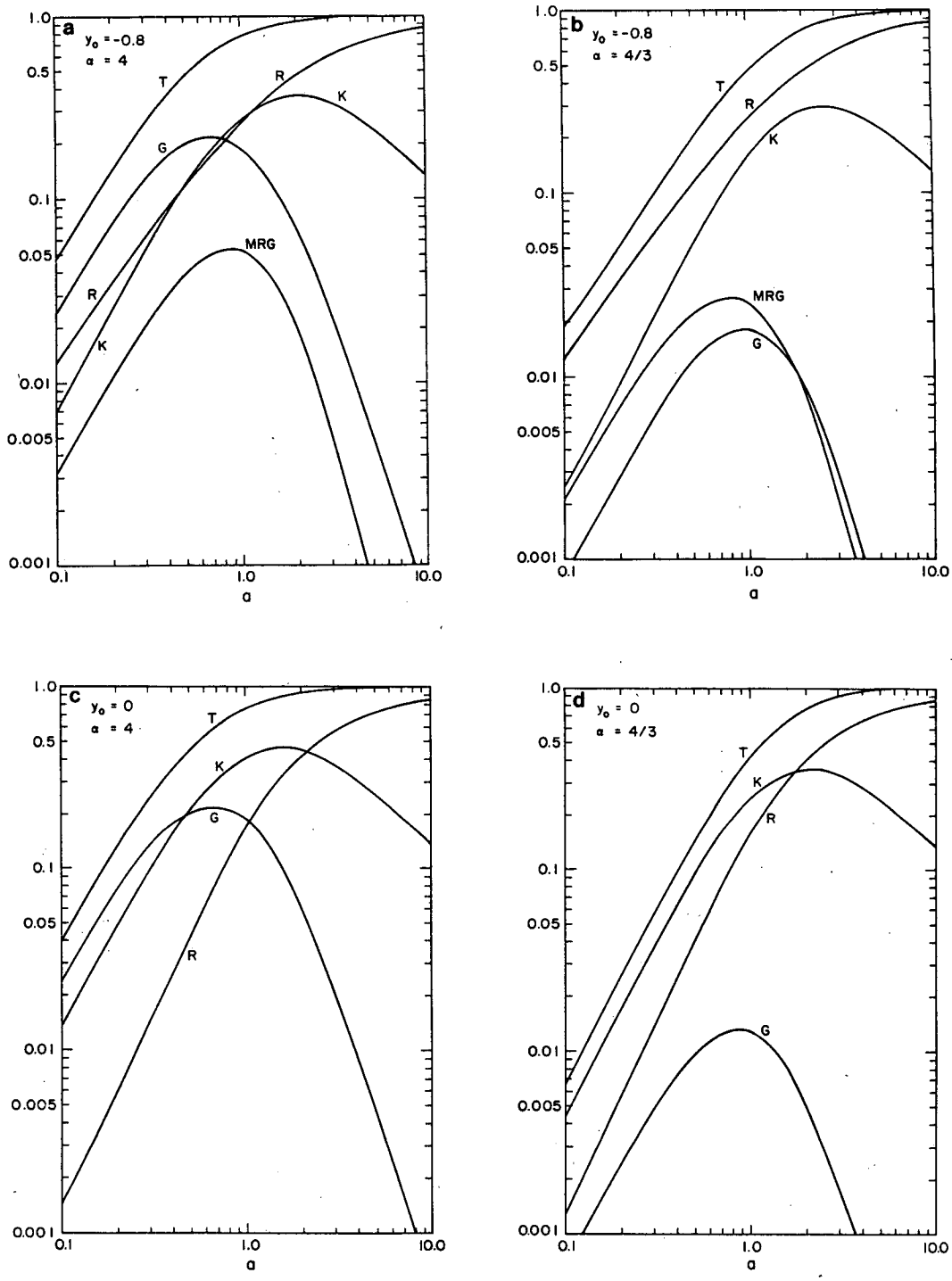

FIG. 3. The normalized modal energy partitions in the limit as $t \to \infty$ for the case of a heat source centered at latitude y_0 with time parameter α as a function of the e-folding radius of the heat source a. The energy in the Rossby, Kelvin, mixed Rossby–gravity and gravity waves is denoted by R, K, MRG and G, respectively, and T is the total energy.

as a function of the time scale α^{-1}, the e-folding radius a, and the latitude y_0 of the forcing. In this section, the temporal evolution of some particular cases are shown and the results are compared with the observed upper-level flow over South America.

Fig. 4a shows the wind and geopotential fields for

the case when $\alpha = 4/3$, $a = 0.5$ and $y_0 = -0.8$ at $t = 2$, 4, 6 and 8 nondimensional units. Also shown is the contribution to the total field from the Kelvin waves (Fig. 4b), mixed Rossby–gravity waves (Fig. 4c) and Rossby waves (Fig. 4d). The wind and geopotential fields are equally scaled in Fig. 4 with the maximum wind vector corresponding to 0.12 nondimensional units. For the internal mode corresponding to $c = 51$ m s^{-1} the dimensional time scale $[T]$ is 8 h and the spatial scale $[L]$ is $\sim$1500 km. This particular scaling was justified in Section 2 based on the vertical projection of a typical convective heating using an observed temperature profile in the tropical region. Using this scaling, the e-folding radius of the thermal forcing is then 750 km and the latitude of the forcing is 11°S. As can be seen in Fig. 2 for $\alpha = 4/3$, the forcing is a maximum at $t = 1.5$ nondimensional units and becomes negligible after $t = 6$ nondimensional units which corresponds to $t = 12$ h and $t = 48$ h respectively.

Many interesting features can be seen in Fig. 4a which shows the total fields. At $t = 16$ h (left column) the high-pressure center that developed in response to the forcing is displaced slightly south of the maximum forcing. Also noticeable is the asymmetry of the response. There is a strong cross-equatorial flow with the maximum wind speed in the neighborhood of the equator. The flow pattern becomes more geostrophic as the latitude increases in agreement with the larger Coriolis parameter. At $t = 32$ h the forcing has decreased to 25% of its maximum intensity and the flow pattern is becoming more geostrophic although the cross-isobaric flow is still intense near the equator. At $t = 32$ h there are several features that deserve attention: (i) the southerly and southeasterly flow on the northeast side of the anticyclone have become more intense, (ii) the center of the anticyclonic circulation is now displaced west of the maximum forcing, (iii) a trough is beginning to develop east of the anticyclonic circulation, (iv) westerlies have developed along the equator with maximum wind speed at $x = 3000$ km and maximum pressure perturbation displaced slightly towards the Northern Hemisphere and (v) the flow across the equator now has an anticyclonic curvature in the Northern Hemisphere. At $t = 48$ h and $t = 64$ h the above characteristics tend to become more evident except that the cross-equatorial flow north of the main high pressure has decreased and a new region of cross-equatorial flow with a northerly component has developed between $x = 1500$ km and $x = 4500$ km. By $t = 48$ h the forcing has decreased to 4% of its maximum value and the whole flow pattern is slowly dispersing. The main anticyclone is becoming elongated toward the west and a sharp east–west geopotential gradient is forming between the low centered near $x = 1500$ km and the main high. Accordingly, strong winds are also observed in this region. Also noticeable is the rapid eastward drift of the circulation pattern discussed in item (iv).

Comparing Fig. 4a with Fig. 4b shows that the circulation pattern described in item (iv) which propagates rapidly eastward is associated with the Kelvin wave contribution. Thus, the cross-isobaric flow observed on the northeast quadrant of Fig. 4a at $t = 16$ h moves eastward and propagates as a nondispersive wave group. At first it may appear that the Kelvin waves in Fig. 4 are exhibiting a dispersive behavior since the initially narrow disturbance at $t = 16$ h becomes elongated at later times. This, however, is due to the continual generation of Kelvin waves while the forcing is active. After $t = 48$ h when the forcing becomes negligible the Kelvin wave group propagates eastward without changing shape.

The contribution from the mixed Rossby–gravity waves shown in Fig. 4c is small, but is responsible for certain features of the total flow field. The mixed Rossby–gravity waves have a westward phase speed, but propagate energy eastward which can be seen in Fig. 4c as a successive eastward reinforcement of the geopotential and wind maxima. Comparing Fig. 4a with Fig. 4c at $t = 48$ h and $t = 64$ h shows that the northwesterly flow at the equator between $x = 1500$ km and $x = 3000$ km, and the lowering of the geopotential near $y = -1500$ km and $x = 1500$ km in the total solution, are associated with the mixed Rossby–gravity waves. The formation of this trough east of the main anticyclone is also caused partially by the eastward dispersion of short Rossby waves which can be seen by comparing Figs. 4a and 4d at $t = 64$ h. The formation of the low geopotential region at $x = 3000$ km and $y = 2000$ km, which is most evident at $t = 64$ h, is also primarily related to the mixed Rossby–gravity waves with some contribution from the shorter Rossby waves.

Fig. 4d shows the contribution to the total solution from the Rossby waves. Comparing Figs. 4d and 4a after $t = 32$ h shows that the high geopotential configuration which appears in the Northern Hemisphere is a manifestation of the Rossby waves. This high pressure is generated in response to the heat source and migrates westward in the early stages of the transient solution. The pattern continues moving westward after the forcing becomes negligible. This evolution in time can be explained by the group velocity of Rossby waves. The solid lines in the lower portion of Fig. 9 are the frequencies of the Rossby modes for several values of m as a function of the zonal wavenumber k. The zonal component of the group velocity is given by $-\partial\nu/\partial k$ which is the slope of each of the curves. Since the slope of the frequency curves for the Rossby modes changes sign (except for $m = 0$), it is evident that the group velocity is eastward for short Rossby waves and westward for long Rossby waves. Thus, the westward elongation of the geopotential field in Fig. 4d is due to the dispersion of long Rossby waves and the intensification of the east–west gradient of the geopotential field east of the main high is a result of the eastward dispersion

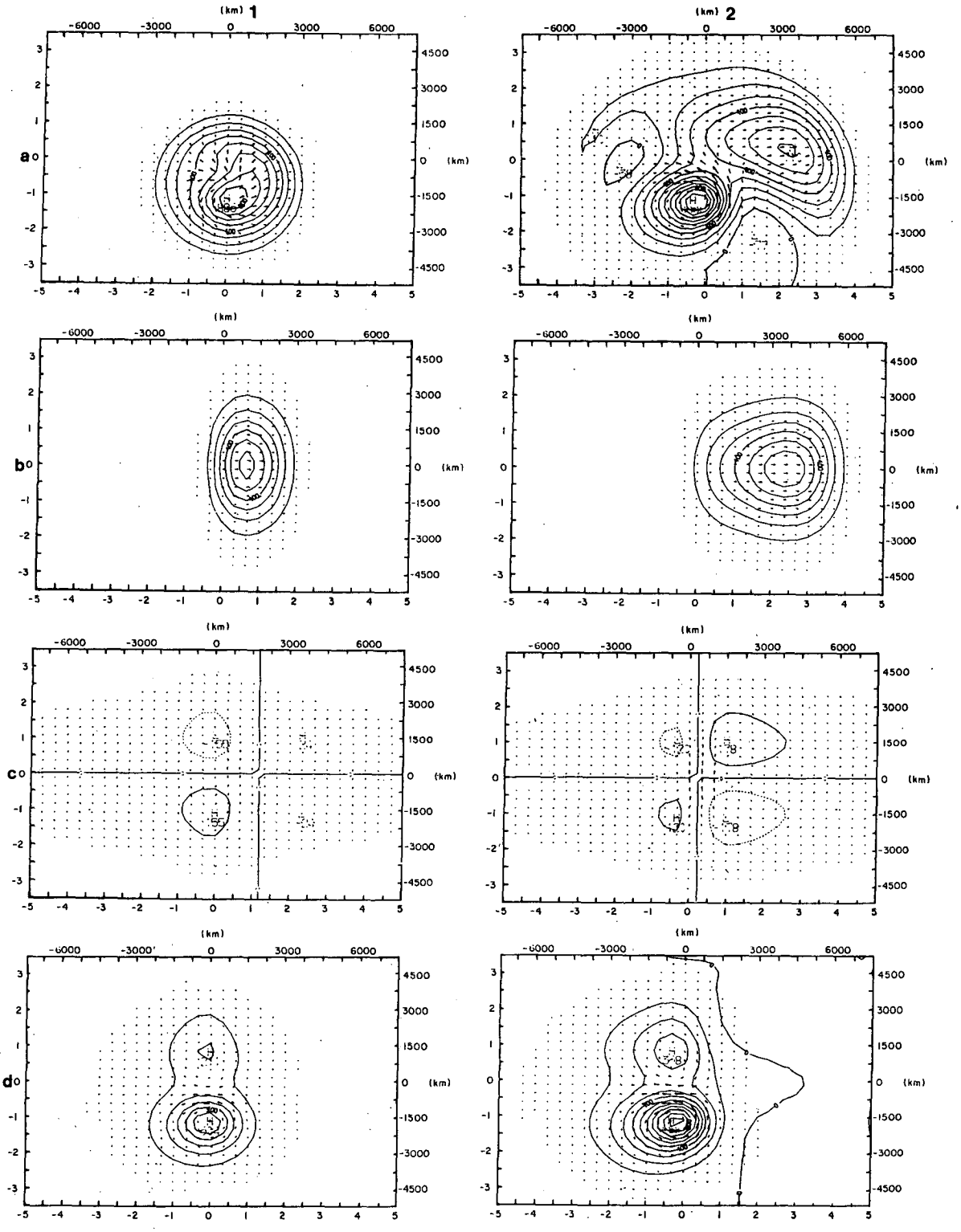

FIG. 4. Horizontal structure of the wind and geopotential fields at t = 16, 32, 48 and 64 h (columns 1, 2, 3 and 4, respectively) for the case of a heat source centered at $y_0 = -1200$ km (11°S) with time constant $\alpha^{-1} = 6$ h and horizontal scale $a = 750$ km. The total field is shown in (a) and the contribution to the total field from the Kelvin, mixed Rossby–gravity and Rossby waves are shown in (b), (c) and (d), respectively.

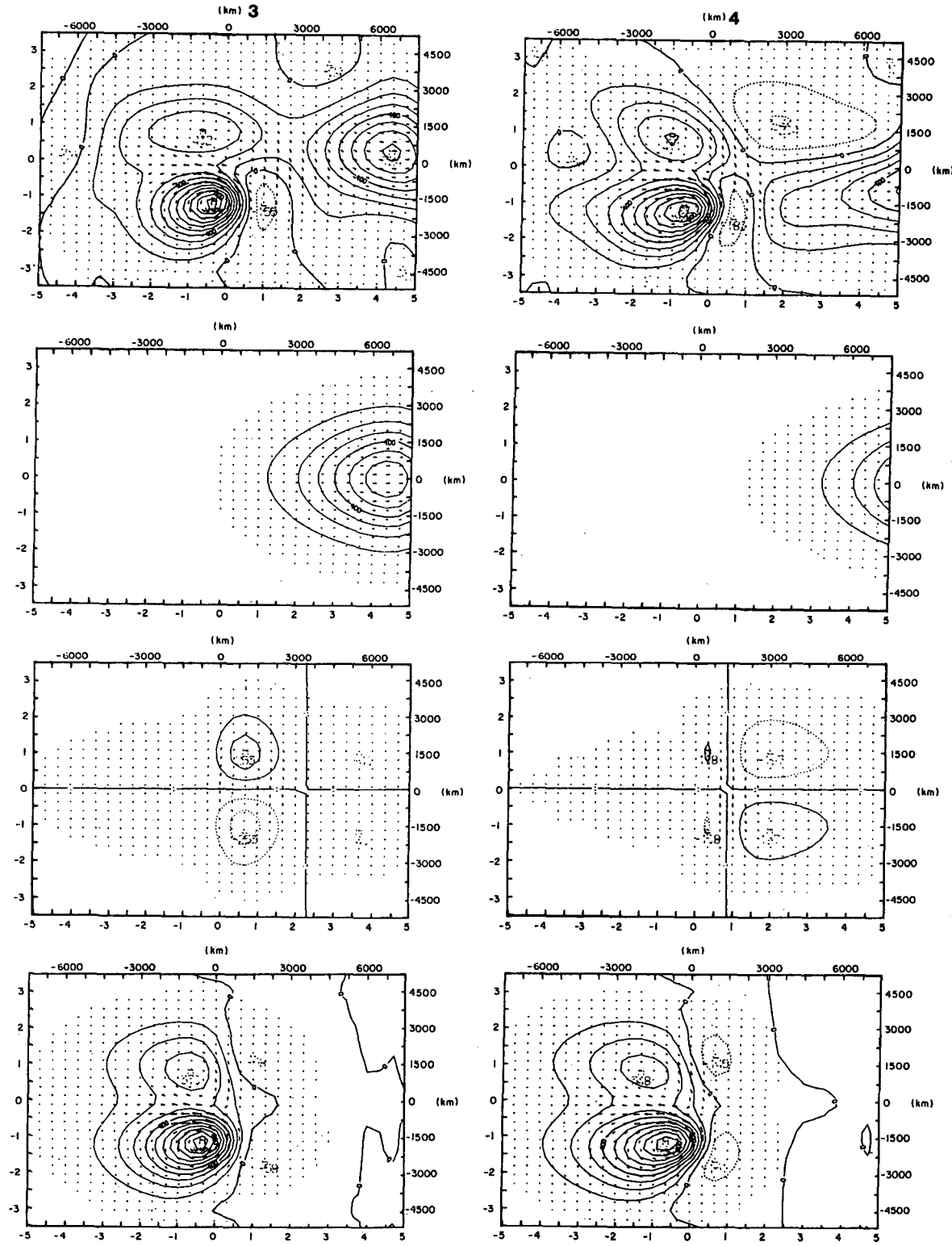

FIG. 4. (*Continued*)

of short Rossby waves. The appearance of a stronger meridional flow at the longitude of maximum forcing is also predictable from the dispersive properties of Rossby waves since short Rossby waves are almost nondispersive and have more kinetic energy in the meridional than in the zonal component of the wind (Longuet-Higgins, 1964; Silva Dias and Schubert, 1979). The strong easterly flow along the equator and the predominately symmetric pattern that develops in Fig. 4a can be associated with the $m = 1$ Rossby mode. This particular mode is expected to have a large contribution to the solution because of its horizontal similarity with the forcing function.

Fig. 5 shows the total wind and geopotential fields for the case when the heat source discussed previously is centered at the equator ($\alpha = \frac{4}{3}$, $a = 0.5$ and $y_0 = 0$). As discussed in Section 3, more of the energy of the final adjusted state is in the Kelvin modes than in the Rossby modes (Fig. 3d). This explains the large amplitude configuration which moves rapidly eastward in Fig. 5. Since the forcing is symmetric about the equator, the initial outward spreading mass builds up two high-pressure centers which are separated by an equatorial trough. During the initial development ($t = 16$ h) it is evident that the mass tends to flow primarily along the equator with the streamlines curving toward the poles and away from the heat source. After the Kelvin waves propagate toward the east, the symmetric Rossby waves which remain in the region of the heat source slowly disperse.

The fields shown in Fig. 5 differ somewhat from the case where the equatorial heat source is stationary in time as discussed by Gill (1980). The stationary case shows a zone of upper-level westerlies to the east of the forcing which is much more extensive than the zone of upper easterlies to the west of the forcing. Gill pointed out that the continual generation of the Kelvin waves by the stationary forcing coupled with the large eastward group velocity of the Kelvin waves compared to the westward group velocity of the long Rossby waves, explained the relative sizes of the east–west circulations. In the transient case shown in Fig. 5 the forcing becomes negligible after $t = 48$ h so that very little Kelvin wave energy is being generated. The pre-

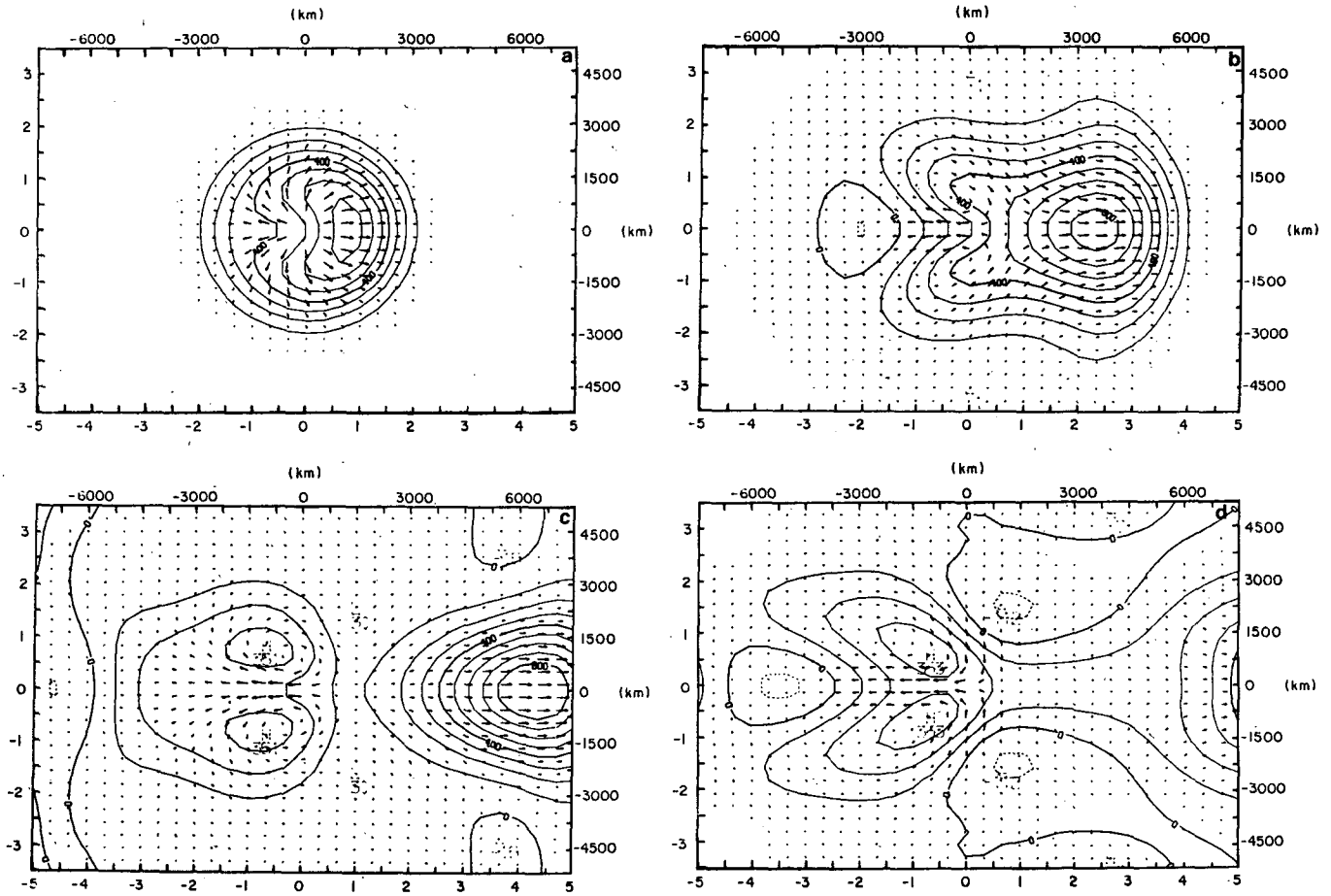

FIG. 5. Horizontal structure of the wind and geopotential fields at $t = 16$, 32, 48 and 64 h [(a), (b), (c) and (d), respectively], for the case of a heat source centered at the equator with time constant $\alpha^{-1} = 6$ h and horizontal scale $a = 750$ km.

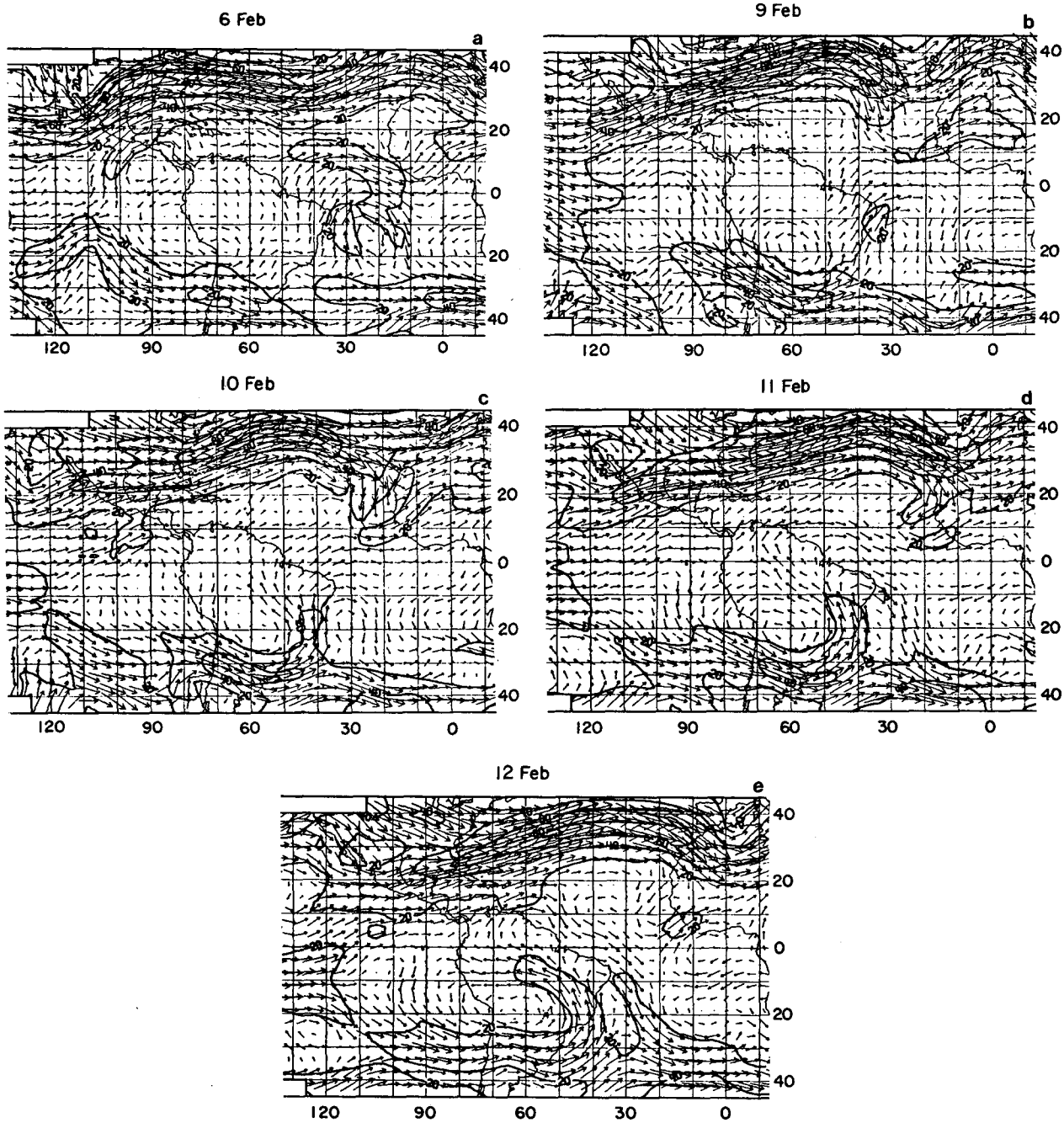

FIG. 6. ECMWF 200 mb maps for 0000 GMT 6 February (a) and for 0000 GMT 9–12 February 1979: (b)–(e) respectively.

viously generated Kelvin waves propagate to the east leaving only the upper-level easterly flow to the west of the forcing which is associated with the slower propagating Rossby waves.

The simulations presented in Figs. 4 and 5 show the response of the model to a transient heat source centered at two different latitudes. For comparison, Fig. 6 shows 200 mb FGGE maps at 0000 GMT for 6 February and for 9–12 February 1979 prepared by the European Centre for Medium Range Weather Forecasting (ECMWF). During a period of 2–3 days before 6 February, the Bolivian high was not well-developed and the main synoptic feature in the equatorial region of South America was an upper-level cyclone off the northeast coast of Brazil. This is the type of upper low studied by Kousky and Gan (1981). After 6 February, the anticyclonic circulation began to organize and during the period 9–12 February (Figs. 6b–

6e), the Bolivian high was again established. On 10 February there was a strong cross-equatorial flow at 50°W which turned and became a westerly flow at about 30°W. The most significant change occurred between 10 and 11 February with the sudden increase in speed of the southerly component between the center of the Bolivian high and the upper trough off the northeast coast of Brazil. On 10 February the cross-equatorial flow was well established and the anticyclonic circulation was developing in the Northern Hemisphere as a result of the change in sign of the Coriolis parameter. The trough off the northeast coast of Brazil was elongated and tilted northwest to southeast. On 12 February the Bolivian high was stretched in the east–west direction with the flow more zonal in the vicinity of the equator and with the wind stronger in the eastern and northeastern sectors of the Bolivian high.

The model results shown in Fig. 4 and Fig. 5 reproduce some of the transient aspects of the Bolivian high. As noted by Virji (1981), a southerly component of the wind dominates over most of the region east and north of the Bolivian high. This is evident in the 9–12 February period shown in Fig. 6, and can also be seen in the model results shown in Fig. 4a. The model results indicate that initially cross-equatorial flow dominates north of the forcing and that it is replaced by easterly flow as the forcing becomes negligible. A similar feature can be seen in Fig. 6. Between the 9th and 10th cross-equatorial flow is established north of the Bolivian high which turns to easterly flow by the 12th. Virgi (1981) also observed maximum mean wind speeds greater than 10 m s^{-1} and exceeding 25 m s^{-1} on certain days within the latitudinal band between 5 and 10°S. The model results indicate that this equatorial easterly jet appears when the Rossby wave component of the solution becomes dominant after the forcing becomes negligible.

As is shown in Fig. 6, the Bolivian high has become elongated in the east–west direction and has maximum winds to the northeast by 12 February. These features were also seen in the model results shown in Fig. 4. The westward elongation of the main high was caused by the westward dispersion of long Rossby waves while the sharp geopotential gradient and large wind speeds to the east were caused by the eastward dispersion of short Rossby waves.

The model results also showed the formation of a trough east of the main high cell. The modal decomposition shown in Fig. 4 indicated that this was a manifestation of the eastward dispersion of the Rossby and mixed Rossby–gravity waves emanating from the source region. A similar trough east of the Bolivian high can be seen in Fig. 6 which gradually sharpens up and acquires a NW–SE tilt between the 9th and 12th.

The anticyclonic flow which developed in the Northern Hemisphere in the model also has its counterpart in the observed flow shown in Fig. 6. As can be seen in Fig. 6 on the 12th, the anticyclonic circulation in the Northern Hemisphere is closer to the equator than the model-produced anticyclone in Fig. 4. The observed anticyclone also shows a larger wind speed on its poleward side than the model results. This difference might be attributed to interaction with the Northern Hemisphere westerlies or possibly to the active convection that usually develops near the equator along the Pacaraima mountain range on the northern border of the Amazon basin.

The relatively strong northerly wind observed on the western sector of the Bolivian high in Fig. 6 is also not reproduced by the transient solution of our simple model. This observed strong northerly wind off the west coast of South America may be a result of the interaction between the anticyclonic circulation over South America and the westerlies over the South Pacific Ocean.

5. Implications for the initialization of tropical models

The existence of Kelvin wave structures emanating from tropical regions of transient convection poses an interesting question about initialization procedures in tropical forecast models. A part of nonlinear normal mode initialization techniques (Machenhauer, 1977; Baer, 1977; Baer and Tribbia, 1977; Daley, 1981) consists of a diagnostic relation between the gravitational and rotational components of the motion. As discussed by Leith (1980), the inclusion of heating and friction in the model equations means that these effects should also appear in the diagnostic initialization relation. In the simple problem considered here, nonlinear normal mode initialization[5] might proceed as follows. First we divide (2.27) into a slow (low-frequency) mode part and a fast (high-frequency) mode part, i.e.

$$\frac{dW_{m,s}}{dt} - i\nu_{m,s}W_{m,s} = \tilde{W}_{m,s}\tfrac{1}{2}\alpha^3 t^2 e^{-\alpha t}, \quad (5.1a)$$

$$\frac{dW_{m,f}}{dt} - i\nu_{m,f}W_{m,f} = \tilde{W}_{m,f}\tfrac{1}{2}\alpha^3 t^2 e^{-\alpha t}. \quad (5.1b)$$

As in Tribbia (1979), we must somewhat arbitrarily choose a frequency which separates the fast and the slow modes. One possibility is that $|\nu_{m,r}| \leqslant 2^{-1/2}$ defines slow modes and $|\nu_{m,r}| > 2^{-1/2}$ defines fast modes. This separation frequency is marked by the intersection of the Kelvin mode and the mixed Rossby–gravity mode in Fig. 9.

Suppose we have an observed initial distribution of geopotential and wind at $t = t_i$. We can project this initial condition onto the normal modes to obtain $W_{m,s}(k, t_i)$ and $W_{m,f}(k, t_i)$, the first of which we retain and the second of which we discard. However, we do

[5] Although our problem is linear we use the terminology "nonlinear normal mode initialization" because of the inclusion of forcing.

not set $W_{m,f}(k, t_i)$ equal to zero, but rather proceed on the belief that the atmosphere has evolved so that it is close to Leith's slow manifold, i.e., $dW_{m,f}/dt$ is small enough that (5.1b) yields

$$W_{m,f}(k, t_i) = \frac{i\tilde{W}_{m,f}(k)}{\nu_{m,f}} \tfrac{1}{2}\alpha^3 t_i^2 e^{-\alpha t_i}, \qquad (5.2)$$

which is the initialization relation for the fast modes. In this type of initialization procedure the past history of the fast modes is ignored since only the current projection of the forcing determines the fast mode component.

Now suppose that this initialization procedure is applied in the middle of one of the simulations of Section 4. How might the subsequent evolution be changed? Fig. 7 is an energy partition diagram with axes $\mathcal{E}_f$ and $\mathcal{E}_s$, where the energies [normalized as in (3.5)–(3.9)] are in the fast and slow modes, respectively. The energy partition for the simulation shown in Fig. 4 ($a = 0.5$, $\alpha = \frac{4}{3}$, $y_o = -0.8$) is denoted by the curve $\mathcal{S}$, in Fig. 7, with the dots indicating equally spaced points in time (every 4 h). The energy in fast modes in simulation $\mathcal{S}$ increases rapidly initially, reaches a maximum, and then decreases while the energy in slow modes increases throughout the simulation. Eventually, a fixed point is approached as the forcing decays to zero. It is interesting to note that there is less fast mode energy in the final state ($t = \infty$) than there was at previous times during the simulation. This indicates that the forcing can remove fast mode energy if the fast mode contribution to the temperature field has cold air in the region of heating. The curve $\mathcal{M}$ in Fig. 7 shows the energy partition when the amplitudes of the slow modes are the same as in $\mathcal{S}$ and the amplitudes of the fast modes are calculated using (5.2). Along curve $\mathcal{M}$, the energy in fast modes reaches a maximum when the forcing is a maximum ($t = 12$ h) and approaches zero as the forcing decays. When nonlinear normal mode initialization is applied to data from $\mathcal{S}$ at $t_i = 16$ h, the model state is brought to a point on $\mathcal{M}$, after which evolution occurs along the forecast curve $\mathcal{F}_N$. Linear normal mode initialization eliminates all the energy in fast modes which brings the model state to a point along the $\mathcal{E}_s$ axis and evolution occurs along $\mathcal{F}_L$. In both cases, the initial balancing procedure results in a reduced contribution from the fast modes, but more energy in the fast modes is eventually generated for the linear initialization case. The nonlinear initialization procedure reduces the total energy by 30% while the linear initialization procedure reduces the total energy by 52% when applied at $t_i = 16$ h. This indicates that it may be difficult to accurately determine an initial condition in regions where there is forcing which has a large projection onto the fast modes.

In order to further understand how close the slow manifold $\mathcal{M}$ is to the simulation $\mathcal{S}$, Fig. 8 displays the physical space fields for $\mathcal{S}$ at $t = 16$ and 32 h and the corresponding fields after nonlinear normal mode initialization has been applied (i.e., Figs. 8a and 8b correspond to points along curve $\mathcal{S}$ in Fig. 7, while Figs. 8c and 8d correspond to points along curve $\mathcal{M}$). The initialization causes some distortion in the geopotential field when applied at $t_i = 16$ h. At $t_i = 32$ h the amplitude of the disturbance to the east of the forcing has been greatly reduced. This disturbance, which is mainly composed of Kelvin modes, is reduced since it has propagated to a region where the forcing is small and the initialization procedure calculates the energy in the fast modes assuming a balance between the forcing and the fast modes. Although this disturbance was generated by the forcing, it was produced before the initialization time, so it cannot be balanced by the forcing at the initialization time.

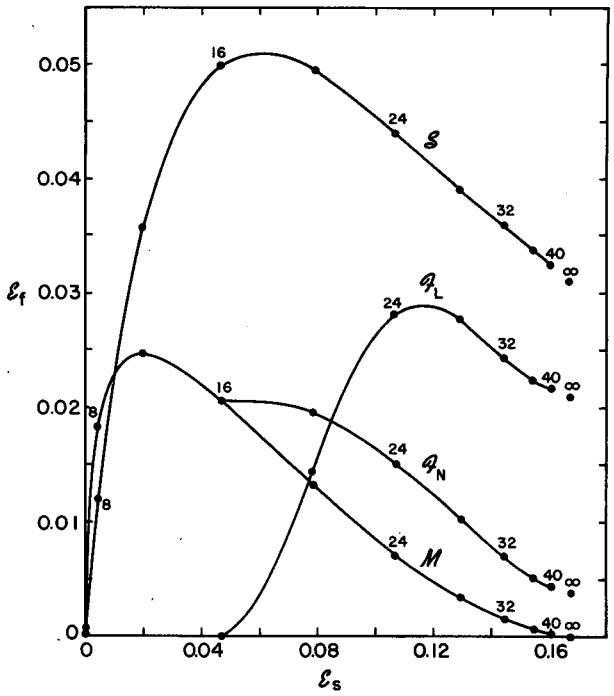

FIG. 7. Energy partition diagram where the abscissa and the ordinate are the energy in the slow modes $\mathcal{E}_s$ and the energy in the fast modes $\mathcal{E}_f$. The curve $\mathcal{S}$ shows the model states for the simulation with $y_0 = -1200$ km, $\alpha^{-1} = 6$ h and $a = 750$ km where the dots indicate equally spaced points in time (every 4 h). Curve $\mathcal{M}$ is the state the model would be brought to if nonlinear normal mode initialization were applied at any time during the simulation. The curves $\mathcal{F}_L$ and $\mathcal{F}_N$ are the forecast states after linear or nonlinear initialization are applied at $t = 16$ h.

6. Concluding remarks

The atmospheric response to transient heat sources in the tropical region has been investigated. Convective bursts have been simulated using the linearized equations for a stratified fluid on an equatorial β-plane with a specified heat source. The model equations have been

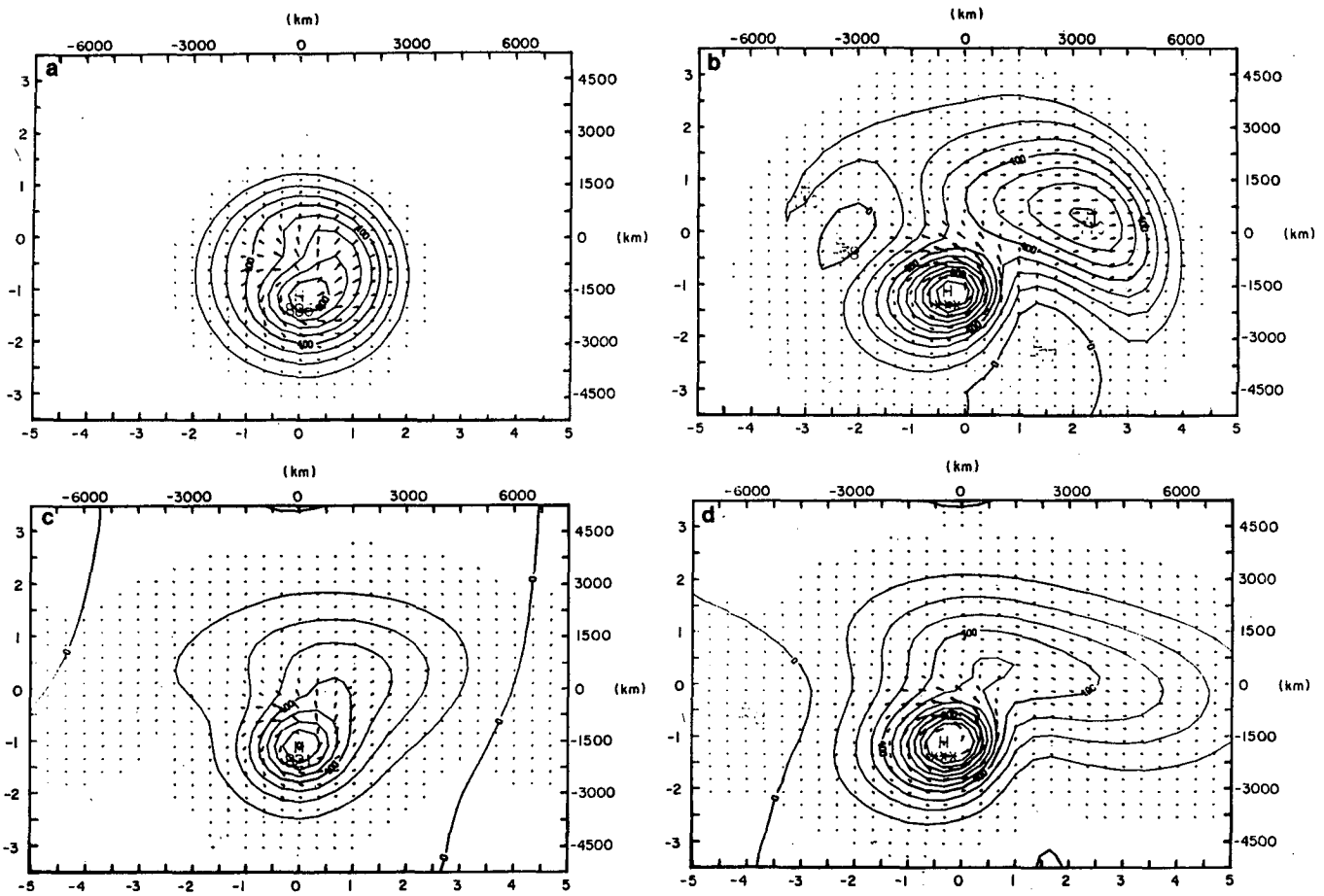

FIG. 8. Wind and geopotential fields before and after nonlinear normal mode initialization is applied. The simulation $y_0 = -1200$ km, $\alpha^{-1} = 6$ h and $a = 750$ km at $t = 16$ h and $t = 32$ h is shown in (a) and (b) and the corresponding fields after the initialization is applied at $t = 16$ h and $t = 32$ h are shown in (c) and (d).

solved using transform techniques, with only the first internal vertical mode being considered. For this case, the governing equations are analogous to shallow water equations.

The results presented in Sections 3 and 4 show that the response of the model to the heat source depends on which of the basic types of waves permitted in the model are generated. The high-frequency modes of the model tend to disperse energy away from the region of the forcing while the lower-frequency modes tend to leave a slowly dispersing flow field in the region of the forcing. It is shown that the spatial and temporal scales, as well as the latitude of the forcing affect the partition of the energy between the fast and slow modes, with the fast modes being favored as the forcing becomes more rapid, closer to the equator and smaller in size.

In Section 4, results were presented from a model simulation using a heat source centered at 11°S with an *e*-folding radius of 750 km and a time scale of about one day. This heat source excites the Kelvin waves of the model which propagate rapidly toward the east, leaving the Rossby and mixed Rossby-gravity wave contribution to the solution in the region of the forcing. The results from this simulation reproduce many of the transient aspects of the Bolivian high. The agreement between the model results and the observations suggests that the release of latent heat has a large effect on the upper tropospheric circulation over tropical South America, as was indicated by Kousky and Kagano (1981). This agreement also indicates that many aspects of the upper tropospheric circulation in this region can be explained by considering the dispersive properties of the Rossby and mixed Rossby-gravity waves as discussed in Section 4.

The Kelvin mode contribution to the transient adjustment problem raises some interesting questions about the dynamics of the equatorial region. As was discussed in Section 3, the amount of Kelvin wave energy generated is greater when the forcing is rapid and when the heat source is close to the equator. The convection that occurs over the South American continent and also over the Indonesian region has large variations on short time scales. Since both of these

regions are close to the equator, there should be a large Kelvin wave response to this convective forcing. Fig. 4b shows that in the upper levels, convergence occurs on the eastern side of the Kelvin wave group with divergence on the western side. This convergence–divergence pattern and associated vertical motion field may be important for modulating convection in areas far to the east of the forcing. There is some observational evidence for this modulation of convection by the Kelvin waves. Lau (1982) has presented a study of satellite cloud imagery from 1 December 1974–31 January 1975 in the area between 90–180°E and 10°N–10°S. In Lau's study, the convective activity over Borneo was often enhanced in association with cold surges from the Northern Hemisphere. After the surge, a region of enhanced convective activity which was symmetric about the equator could be identified for up to six days as it propagated toward the east. A feature similar to this has also been observed by Williams (1981).

The generation of Kelvin waves by transient convection has some implications for the initialization of tropical forecast models. The basic idea of many nonlinear normal mode initialization procedures is to obtain the slow mode part of an initial field from observations, and then to diagnose the fast mode part in such a way that the initial tendency of the fast modes is zero. When this type of procedure is applied, the magnitude of the nonlinear interaction of the slow modes and the magnitude of the forcing terms at the initialization time determine the amplitude of the fast modes. For the case of transient convection, the amplitude of the Kelvin modes will be fairly large after the amplitude of the forcing has decreased. Since the Kelvin waves are considered to be fast modes (except for very long waves), it may not be possible to diagnose these after the magnitude of the forcing has decreased and the waves have propagated away from the source region.

As discussed previously, the time and space scales of the heat source affect the response of the model. It should be emphasized that these scales are a function of the vertical structure of the heating. In the current model formulation, the time and length scales were based on the first internal mode, since the vertical structure of Yanai's apparent heat source is associated with deep convection and has a large projection onto this mode. In different geographic areas, the vertical structure of the apparent heat source might be different than the structure of Yanai's heat source so that other vertical modes may also be important. Further work is needed in this area to evaluate the applicability of the single equivalent depth analysis and the nature of the forcing which drives the tropical circulation.

Acknowledgments. The authors are grateful to Scott Fulton, William Gray, Richard Johnson, Akira Kasahara, Vern Kousky, Maria Silva Dias, Duane Stevens and Joseph Tribbia for their valuable comments on this problem. We are also indebted to Odilia Panella for her help in preparing the manuscript. Research support for WHS and MD has been provided by NSF Grant ATM-8207563 and for PLS by NOAA P.O. No. NA82AAG00927.

APPENDIX A

The Vertical Transform

The only z derivatives appearing in the governing equations (2.6)–(2.8) are those in the first and last terms of (2.8), which can be combined into

$$e^z \frac{\partial}{\partial z}\left[\frac{e^{-z}}{R\Gamma}\frac{\partial}{\partial z}(\phi - \tilde{\phi})\right]. \tag{A1}$$

We consider the finite Stürm-Liouville transform of the function $f(x, y, z, t)$,

$$f_n(x, y, t) = \int_0^{z_T} f(x, y, z, t)\Psi_n(z)e^{-z/2}dz, \tag{A2}$$

where $e^{-z/2}$ is the weight and Ψ_n is the kernel of the transform. We now attempt to discover the form of Ψ_n which is most convenient for our problem, i.e., the one which allows (A1) to be transformed, subject to boundary conditions (2.9), into a constant times $\phi_n - \tilde{\phi}_n$. Taking the transform of (A1) and integrating by parts twice, we obtain

$$\int_0^{z_T} \Psi_n(z)e^z \frac{\partial}{\partial z}\left[\frac{e^{-z}}{R\Gamma}\frac{\partial}{\partial z}(\phi - \tilde{\phi})\right]e^{-z/2}dz$$

$$= \left[\frac{e^{-z}}{R}\left\{e^{z/2}\Psi_n\frac{\partial}{\partial z}(\phi - \tilde{\phi}) - \frac{\partial e^{z/2}\Psi_n}{\partial z}(\phi - \tilde{\phi})\right\}\right]_0^{z_T}$$

$$+ \int_0^{z_T} (\phi - \tilde{\phi})e^{z/2}\frac{\partial}{\partial z}\left[\frac{e^{-z}}{R\Gamma}\frac{\partial e^{z/2}\Psi_n}{\partial z}\right]e^{-z/2}dz. \tag{A3}$$

If we choose $\Psi_n(z)$ to be the solution of the Stürm-Liouville problem

$$e^{z/2}\frac{\partial}{\partial z}\left(\frac{e^{-z}}{R\Gamma}\frac{\partial e^{z/2}\Psi_n}{\partial z}\right) + \frac{1}{gh_n}\Psi_n = 0, \tag{A4a}$$

$$\frac{\partial e^{z/2}\Psi_n}{\partial z} - \frac{\Gamma}{\bar{T}}e^{z/2}\Psi_n = 0 \quad \text{at} \quad z = 0, \tag{A4b}$$

$$\frac{\partial e^{z/2}\Psi_n}{\partial z} = 0 \quad z = z_T, \tag{A4c}$$

and if we use the boundary conditions (2.9), then (A3) becomes

$$\int_0^{zT} \Psi_n(z) e^z \frac{\partial}{\partial z}\left[\frac{e^{-z}}{R\Gamma}\frac{\partial}{\partial z}(\phi - \tilde{\phi})\right] e^{-z/2} dz = -\frac{1}{gh_n}(\phi_n - \tilde{\phi}_n). \quad \text{(A5)}$$

This is the desired operational property of the Stürm-Liouville transform whose kernel is defined by (A4).

APPENDIX B

The Meridional Transform

We first prove that the operator $\hat{\mathbf{L}}$ is skew-Hermitian. Consider the complex, three-component vectors **f** and **g**. Using (2.20) we can write

$$(\hat{\mathbf{L}}\mathbf{f}, \mathbf{g}) = \int_{-\infty}^{\infty} \left[(-yf_2 + ikf_3)g_1^* + \left(yf_1 + \frac{\partial f_3}{\partial y}\right)g_2^* + \left(ikf_1 + \frac{\partial f_2}{\partial y}\right)g_3^*\right] dy. \quad \text{(B1)}$$

After integration by parts, rearrangement, and use of (2.24) we obtain

$$(\mathbf{f}, \mathbf{L}^\dagger \mathbf{g}) = \int_{-\infty}^{\infty} \left[f_1(yg_2^* + ikg_3^*) + f_2\left(-yg_1^* - \frac{\partial g_3}{\partial y}\right) + f_3\left(ikg_1^* - \frac{\partial g_2^*}{\partial y}\right)\right] dy + [g_2^* f_3 + f_2 g_3^*]_{-\infty}^{\infty}. \quad \text{(B2)}$$

The final term in (B2) vanishes because of the boundary conditions. Then, using (2.20) we conclude that

$$\hat{\mathbf{L}}^\dagger = \begin{pmatrix} 0 & y & -ik \\ -y & 0 & -\dfrac{\partial}{\partial y} \\ -ik & \dfrac{\partial}{\partial y} & 0 \end{pmatrix} = -\hat{\mathbf{L}}, \quad \text{(B3)}$$

i.e., $\hat{\mathbf{L}}$ is skew-Hermitian.

The eigenfunctions of (2.23) form a complete and orthogonal set (Matsuno, 1966; Cane and Sarachik, 1976) in the space of square integrable functions on the interval $(-\infty, \infty)$. The eigenfunctions and eigenvalues were thoroughly discussed by Matsuno (1966) and Lindzen (1967) and can be written

$$\mathbf{K}_{m,r}(k, y) = \begin{cases} \begin{pmatrix} \frac{1}{2}(\nu_{m,r} - k)H_{m+1}(y) + m(\nu_{m,r} + k)H_{m-1}(y) \\ i(\nu_{m,r}^2 - k^2)H_m(y) \\ \frac{1}{2}(\nu_{m,r} - k)H_{m+1}(y) - m(\nu_{m,r} + k)H_{m-1}(y) \end{pmatrix} \dfrac{e^{-1/2y^2}}{\sqrt{E_{m,r}(k)}}, & m \geq 0 \\ \begin{pmatrix} 1 \\ 0 \\ 1 \end{pmatrix} \dfrac{e^{-1/2y^2}}{(2\sqrt{\pi})^{1/2}}, & m = -1 \end{cases}, \quad \text{(B4)}$$

where

$$\begin{cases} \text{For } m > 0, & \nu_{m,r}^2 - k^2 + \dfrac{k}{\nu_{m,r}} = 2m + 1 & r = \begin{cases} 0 & \text{Rossby} \\ 1 & \text{west gravity} \\ 2 & \text{east gravity} \end{cases} & \\ \text{For } m = 0, & \nu_{m,r} = \begin{cases} -\dfrac{k}{2} + \left[\left(\dfrac{k}{2}\right)^2 + 1\right]^{1/2} & r = \begin{cases} 0 \text{ if } k > \dfrac{1}{\sqrt{2}} \\ 1 \text{ if } k < \dfrac{1}{\sqrt{2}} \end{cases} & \text{mixed Rossby–gravity} \\ -\dfrac{k}{2} - \left[\left(\dfrac{k}{2}\right)^2 + 1\right]^{1/2} & r = 2 & \text{east gravity} \end{cases} & \\ \text{For } m = -1, & \nu_{m,r} = -k & r = 2 & \text{Kelvin} \end{cases} \quad \text{(B.5)}$$

If the normalization factor $E_{m,r}(k)$ is defined by

$$E_{m,r}(k) = 2^m m!\sqrt{\pi}[(m+1)(\nu_{m,r} - k)^2 + m(\nu_{m,r} + k)^2 + (\nu_{m,r}^2 - k^2)^2],$$

the eigenfunctions $\mathbf{K}_{m,r}(k, y)$ satisfy the orthonormality condition

$$(\mathbf{K}_{m,r}(k, y), \mathbf{K}_{m',r'}(k, y)) = \begin{cases} 1, & (m', r') = (m, r) \\ 0, & (m', r') \neq (m, r) \end{cases}.$$

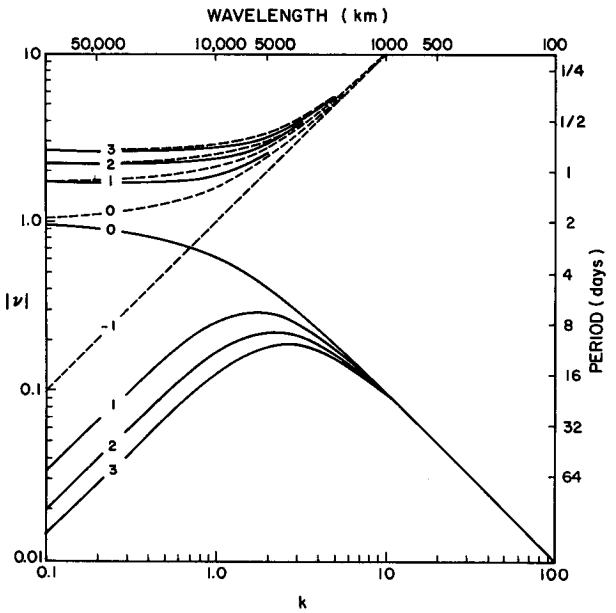

FIG. 9. The absolute value of the eigenfrequencies of the linearized shallow water equations on the equatorial β-plane. The dimensional axes are for a phase speed of the first internal vertical mode.

When $m > 0$ the roots of the dispersion relation have been classified as either a Rossby wave ($r = 0$), a westward gravity wave ($r = 1$), or an eastward gravity wave ($r = 2$). When $m = 0$, the $\nu = k$ root must be discarded. Of the two remaining roots, one is negative and one is positive. The negative root has been classified as an eastward gravity wave ($r = 2$), while the positive root, or mixed Rossby–gravity wave, is classified as a gravity wave ($r = 1$) if $k < 2^{-1/2}$ and as a Rossby wave ($r = 0$) if $k \geq 2^{-1/2}$. Finally, when $m = -1$, the only root is classified as a Kelvin wave. Solutions of the dispersion relation (B5) are shown in Fig. 9.

REFERENCES

Baer, F., 1977: Adjustments of initial conditions required to suppress gravity oscillations in nonlinear flows. *Contrib. Atmos. Phys.*, **50,** 350–366.

——, and J. Tribbia, 1977: On complete filtering of gravity modes through nonlinear initialization. *Mon. Wea. Rev.*, **105,** 1536–1539.

Cane, M., and E. S. Sarachik, 1976: Forced baroclinic ocean motions. Part I. The linear equatorial unbounded case. *J. Mar. Res.*, **34,** 629–665.

Daley, R., 1981: Normal mode initialization. *Rev. Geophys. Space Phys.*, **19,** 450–468.

Erdelyi, A., W. Magnus, F. Oberhettinger and F. G. Tricomi, 1954: *Tables of Integral Transforms,* 2 Vols. McGraw-Hill, 842 pp.

Geisler, J. E., and D. E. Stevens, 1982: On the vertical structure of damped steady circulation in the tropics. *Quart. J. Roy. Meteor. Soc.*, **108,** 87–93.

Gill, A. E., 1980: Some simple solutions for heat induced tropical circulation. *Quart. J. Roy. Meteor. Soc.*, **106,** 447–462.

——, 1982: *Atmosphere-Ocean Dynamics.* Academic Press, 662 pp.

Kasahara, A., 1977: Numerical integration of the global barotropic primitive equations with Hough harmonic expansions. *J. Atmos. Sci.*, **34,** 687–701.

Kousky, V. E., 1979: Frontal influences on northeast Brazil. *Mon. Wea. Rev.*, **107,** 1140–1153.

——, 1980: Diurnal rainfall variation in northeast Brazil. *Mon. Wea. Rev.*, **108,** 488–498.

——, and M. A. Gan, 1981: Upper tropospheric cyclonic vortices in the tropical South Atlantic. *Tellus,* **33,** 538–550.

——, and M. T. Kagano, 1981: A climatological study of the tropospheric circulation over the Amazon region. *Acta Amazonica,* **11,** 743–758.

Kreuels, R., K. Fraedrich and E. Ruprecht, 1975: An aerological climatology of South America. *Meteor. Rundsch.*, **28,** 17–24.

Lau, K.-M., 1982: Equatorial response to northeasterly cold surges as inferred from satellite cloud imageries. *Proc. Int. Conf. Scientific Results Monsoon Experiment,* WMO/ICSU, 5–37.

——, and H. Lim, 1982: Thermally driven motions in an equatorial β-plane: Hadley and Walker circulations during the winter monsoon. *Mon. Wea. Rev.*, **110,** 336–353.

Leith, C., 1980: Nonlinear normal mode initialization and quasi-geostrophic theory. *J. Atmos. Sci.*, **37,** 958–968.

Lim, H., and C.-P. Chang, 1981: A theory of midlatitude forcing of tropical motions during winter monsoons. *J. Atmos. Sci.*, **38,** 2377–2392.

Lindzen, R. S., 1967: Planetary waves on beta-planes. *Mon. Wea. Rev.*, **95,** 441–451.

Longuet-Higgins, M. S., 1964: On group velocity and energy flux in planetary wave motions. *Deep-Sea Res.*, **11,** 35–42.

Machenhauer, B., 1977: On the dynamics of gravity oscillations in a shallow water model with applications to normal mode initialization. *Contrib. Atmos. Sci.*, **50,** 253–271.

Matsuno, T., 1966: Quasi-geostrophic motions in the equatorial area. *J. Meteor. Soc. Japan,* **44,** 25–43.

Paegle, J., 1978: The transient mass-flow adjustment of heated atmospheric circulations. *J. Atmos. Sci.*, **35,** 1678–1688.

Silva Dias, P. L., and W. H. Schubert, 1979: The dynamics of equatorial mass-flow adjustment. Atmos. Sci. Pap. No. 312, Colorado State University, Fort Collins, 203 pp.

Tribbia, J. J., 1979: Nonlinear initialization on an equatorial beta-plane. *Mon. Wea. Rev.*, **107,** 704–713.

Virgi, H., 1981: A preliminary study of summertime tropospheric circulation patterns over South America estimated from cloud winds. *Mon. Wea. Rev.*, **109,** 599–610.

Webster, P. J., 1972: Response of the tropical atmosphere to local, steady forcing. *Mon. Wea. Rev.*, **100,** 518–541.

——, 1973a: Remote forcing of the time-independent tropical atmosphere. *Mon. Wea. Rev.*, **101,** 58–68.

——, 1973b: Temporal variation of low-latitude zonal circulations. *Mon. Wea. Rev.*, **101,** 803–816.

——, 1981: Mechanisms determining the atmospheric response to sea surface temperature anomalies. *J. Atmos. Sci.*, **38,** 554–571.

Williams, M., 1981: Interhemispheric interaction during winter MONEX. *Proc. Int. Conf. Early Results of FGGE and Large-Scale Aspects of its Monsoon Experiments,* WMO, Vol. 10, 12–16.

Yanai, M., S. Esbensen and J.-H. Chu, 1973: Determination of bulk properties of tropical cloud clusters from large-scale heat and moisture budgets. *J. Atmos. Sci.*, **30,** 611–627.